Estimation of rail properties using semi-analytical finite element models and guided wave ultrasound measurements

Isaac I. Setshedi[a,b,*], Philip W. Loveday[b], Craig S. Long[b], Daniel N. Wilke[a]

[a]*University of Pretoria, South Africa*
[b]*CSIR Material Science and Manufacturing, South Africa*

Abstract

Guided wave based monitoring systems require accurate knowledge of mode propagation characteristics such as wavenumber and group velocity dispersion curves. These characteristics may be computed numerically for a rail provided that the material and geometric properties of the rail are known. Generally, the rail properties are not known with sufficient accuracy and these properties also change due to temperature, rail wear and rail grinding. An automated procedure is proposed to estimate material and geometric properties of a rail by finding the properties which, when input into a Semi-Analytical Finite Element (SAFE) model, accurately reproduce measured dispersion characteristics. Pulse-echo measurements were performed and spectrograms show the reflections from aluminothermic welds of three modes of propagation. The SAFE method was used to solve the forward problem of predicting the dispersion characteristics for specified rail properties. Dispersion curves are computed for different combinations of Poisson's ratio and three geometric parameters. These dispersion curves are scaled to cover a range of longitudinal speeds of sound of the rail material. A technique is developed to determine which SAFE model provided the best fit to the experimental measurements. The technique does not require knowledge of the distances to the reflectors; rather these distances are estimated as part of the proposed procedure. A SAFE model with the estimated rail parameters produced dispersion curves and distances in very good agreement with the measured spectrograms. In addition, the estimated mean geometric parameters agreed with the measured profile of the rail head.

Keywords: Inverse problem, Rail, Ultrasonic Guided Waves, Semi-Analytical Finite Element Method, Property Estimation

1. Introduction

Broken rails are one of the leading causes of train derailments worldwide [1]. The relatively large number of rail breaks and resulting train derailments on South African heavy haul lines

---

*Corresponding author.

Email addresses: `u10319965@tuks.co.za` (Isaac I. Setshedi), `PLoveday@csir.co.za` (Philip W. Loveday), `CLong@csir.co.za` (Craig S. Long), `nico.wilke@up.ac.za` (Daniel N. Wilke)

led to the development of a guided wave ultrasound (GWU) based monitoring system to detect broken rails. The system operates in pitch - catch mode with alternate transmit and receive stations permanently installed along the continuously welded rail track. A guided wave mode with energy concentrated mainly in the head of the rail allows distances of up to 2km between the transmitter and receiver stations [2]. The system is primarily a broken rail detector although defects are sometimes detected before complete breakage of the rail occurs. Research is currently being performed to upgrade the system to detect defects prior to broken rails. This will be achieved by the addition of a pulse-echo mode of operation which will allow defects such as cracks to be detected, located along the length of rail track and possibly even monitored. In common with other guided wave based systems, the task is complicated by the presence of numerous guided wave modes and dispersion. Signal processing such as dispersion compensation and phased array processing have been applied to experimental measurements [3]. This signal processing requires an accurate model of the dispersion characteristics of the rail that is being monitored.

The Semi-Analytical Finite Element (SAFE) method has become popular for the computation of dispersion characteristics of waveguides with arbitrary but constant cross-sections such as rails [4, 5, 6, 7, 8]. The method can efficiently predict the dispersion characteristics provided that the material properties and geometry are known. The elastic modulus of the rail material at the frequencies of operation is generally not available and can depend on temperature [9]. In addition, the geometry of the rail head changes due to wear and regular maintenance during the operational lifespan of the rail. Rail wear is dependent on contact stresses and sliding or sticking conditions in the wheel-rail rolling contact area [10]. Studies have been conducted to predict the evolution of the rail profile for various conditions [10, 11, 12, 13] and these studies highlight the complex nature of this evolution. Maintenance operations on the rail include profile grinding, which is performed to restore the profile of the head of the rail and to remove or curtail the length of rolling contact fatigue cracks [14]. It is possible to measure some of the dispersion characteristics using the monitoring equipment.

In continuously welded rail track, sections of rail are welded together in the field using aluminothermic welding and a weld cap remains in place. This weld cap produces a reflection of ultrasonic guided waves and these reflections can be used to measure dispersion characteristics of some modes of propagation. Figure 1a illustrates a transducer attached to the head of the rail and the presence of aluminothermic welds at regular distances and represents the experimental setup used in this work. Figure 1a also indicates that weld reflections can originate on either side of the transducer since the excited waves propagate in both the forward and backward directions. Figure 1b shows a photograph of a typical weld cap. The distances between the welds can be up to 240m but these distances are not accurately known.

The objective of this research was to solve the inverse problem of finding rail material and geometric parameters that, when used as input parameters in a SAFE model, reproduce the measured dispersion characteristics as accurately as possible. The SAFE model can then be used to predict additional dispersion characteristics that may be required for the signal processing algorithms. The forward problem involves setting material and geometric input

parameters in a SAFE model and computing the eigenvalue problem at various frequencies to obtain dispersion characteristics. It is expected that the forward problem will be solved numerous times during the solution of the inverse problem and it is therefore important that the forward problem is solved efficiently. In addition, the number of input parameters to be estimated will greatly influence the number of forward problems to be solved and reducing this number of parameters will greatly reduce the effort required to solve the inverse problem. In Section 2 the SAFE method is briefly introduced before a small set of input parameters are proposed. In order to automate the process a mesh movement strategy is described and a mode shape tracking method is developed to identify the experimentally measured modes in the SAFE dispersion predictions.

Section 3 describes the solution of the inverse problem. Measured pulse-echo signals are shown as time-frequency spectrograms and reflections of specific modes of propagation are identified. Latin Hypercube Sampling is used to select a set of input parameter combinations for solution of the forward problem. A technique is developed to determine which SAFE model best fits the measured spectrograms. This technique uses the dispersion characteristics from each SAFE model to transform the measured spectrograms and the degree to which the different reflected modes and frequencies align at a single distance for each weld provides a measure of how well the SAFE model fits the experimental data.

The method is applied to two experimental measurements in Section 4 and rail property estimates are presented. Conclusions and recommendations for future research are contained in Section 5.
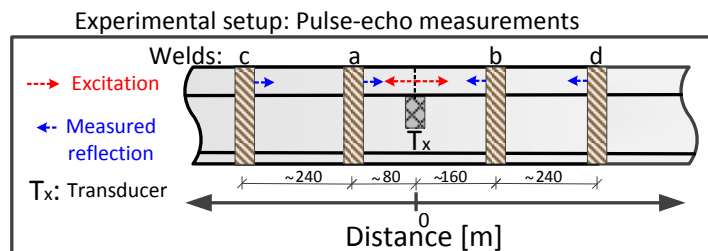
(a)   (b)

Figure 1: (a) Illustration of the experimental setup with estimated weld distances from the transducer location. (b) Photograph of an aluminothermic weld.

2. The SAFE method, selection of parameters and mode shape tracking

In this section a brief description of the SAFE method is provided highlighting aspects that are required in this study. The SAFE mass and stiffness matrices and equation of motion are used to identify a minimum set of material properties to describe the elastic isotropic material. Geometric parameters required to describe the changing rail head due to wear and rail grinding are selected. Finally, a method of identifying the experimentally measured modes in the SAFE results is developed based on mode shapes.

2.1. The SAFE method

In the SAFE method, only the cross-sectional area of the waveguide is discretized with finite elements, while the span or propagation direction is treated analytically. This makes the method highly efficient for computing guided wave dispersion characteristics but requires the assumption that the rail cross-sectional geometry and material properties are constant along the propagation direction. We consider an elastic isotropic rail with wave propagation in the z direction and constant cross-section in the $x - y$ plane. Following the formulation developed by [4] the spatial displacement fields u_x, u_y and u_z in the x, y and $z-$direction, respectively are written as,

$$
\begin{aligned}
u_x(x, y, z, t) &= u_x(x, y)e^{i(\kappa z - \omega t)} \\
u_y(x, y, z, t) &= u_y(x, y)e^{i(\kappa z - \omega t)} \\
u_z(x, y, z, t) &= u_z(x, y)e^{i(\kappa z - \omega t - \pi/2)} = -iu_z(x, y)e^{i(\kappa z - \omega t)}
\end{aligned}
\tag{1}
$$

where, κ and ω are the wavenumber and frequency respectively, and $i = \sqrt{-1}$ is the imaginary unit.

The finite element method is applied to formulate elemental mass and stiffness matrices which are then assembled into global matrices and a matrix eigenvalue problem for free harmonic vibration, given by

$$
\left[\mathbf{K}_1 + i\kappa\mathbf{K}_2 + \kappa^2\mathbf{K}_3 - \omega^2\mathbf{M}\right]\mathbf{Q} = \mathbf{0}
\tag{2}
$$

where $\mathbf{K}_n$, $n = 1, 2, 3$ are stiffness matrices with different relations to wavenumber, $\mathbf{M}$ is the mass matrix and $\mathbf{Q}$ represents the eigenvector. This system of equations differs from that obtained in traditional 3D FEM in that it contains the wavenumber along the waveguide. Propagating modes may be computed from equation (2) by specifying a real wavenumber and solving the eigenvalue problem to obtain real frequencies and mode shapes. Alternately, for computing the wavenumber at a specific frequency, the system of equations may be arranged such that

$$
[\mathbf{A} - \kappa\mathbf{B}]\bar{\mathbf{Q}} = \mathbf{0}
\tag{3}
$$

where

$$
\mathbf{A} = \begin{bmatrix} \mathbf{K}_1 - \omega^2\mathbf{M} & \mathbf{O} \\ \mathbf{O} & -\mathbf{K}_3 \end{bmatrix}, \qquad \mathbf{B} = \begin{bmatrix} -i\mathbf{K}_2 & -\mathbf{K}_3 \\ -\mathbf{K}_3 & \mathbf{O} \end{bmatrix}, \qquad \bar{\mathbf{Q}} = \begin{bmatrix} \mathbf{Q} \\ \kappa\mathbf{Q} \end{bmatrix}
\tag{4}
$$

and $\mathbf{O}$ represents a zero matrix of size $M \times M$. Equation (3) results in $2M$ eigenvalue outputs of M forward and M backward pairs of eigenvalues. Computed eigenvalues may be real, complex or imaginary. Complex and imaginary eigenvalues represent evanescent modes, whereas real eigenvalues represent propagating modes at selected frequencies.

The group velocity, $v_g = \partial\omega/\partial\kappa$, of a propagating mode can be calculated directly at each (κ, ω) solution by evaluating the derivative of the equation of motion, in equation (2), with respect to the wavenumber,

$$v_g = \frac{\partial \omega}{\partial \kappa} = \frac{\mathbf{Q}^T \left(i\mathbf{K}_2 + 2\kappa\mathbf{K}_3\right) \mathbf{Q}}{2\omega\mathbf{Q}^T\mathbf{M}\mathbf{Q}}. \tag{5}$$

Convergence of the group velocity at 40 kHz for different element topologies (three noded triangular, six noded triangular, four noded quadrilatera and eight noded quadrilateral (Q8) element topologies) were conducted to find the best FE discretization of the rail. The Q8 element discretizations showed the best accuracy and convergence properties compared to other element topologies.
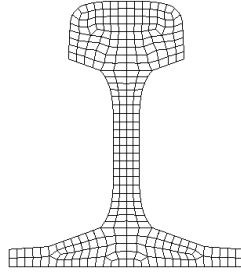

Figure 2: Mesh of quadratic elements used in the SAFE analysis of the UIC60 rail.

Considering that many SAFE model solutions will be required when solving the inverse problem of estimating geometrical and material properties, we do not want the model to be larger than necessary. It was decided that the 1005 noded mesh using Q8 elements, depicted in Figure 2, was sufficient as it resulted in an error below 1% [15].

2.2. Selection of rail material parameters

We consider only a rail with uniform material properties described by a density, an elastic modulus and a Poisson's ratio. The density in each element is the same and it is possible to factor out the density from the global mass matrix as follows:

$$\mathbf{M} = \rho\bar{\mathbf{M}} \tag{6}$$

The elasticity matrix $\mathbf{C}$ is dependent on the elastic modulus E and the Poisson's ratio as shown in equation (7) where it is observed that the elastic modulus can be factored out while the Poisson's ratio cannot be factored out.

$$\mathbf{C} = \frac{E}{(1 + \nu)(1 - 2\nu)} \begin{bmatrix} 1 - \nu & \nu & \nu & & & \\ \nu & 1 - \nu & \nu & & & \\ \nu & \nu & 1 - \nu & & & \\ & & & \frac{1-2\nu}{2} & & \\ & & & & \frac{1-2\nu}{2} & \\ & & & & & \frac{1-2\nu}{2} \end{bmatrix} \tag{7}$$

The stiffness matrices can therefore be written

$$\mathbf{K} = E\bar{\mathbf{K}} \tag{8}$$

5

and the eigenvalue problem is then

$$\left[\bar{\mathbf{K}}_1 + i\kappa\bar{\mathbf{K}}_2 + \kappa^2\bar{\mathbf{K}}_3 - \frac{\rho}{E}\omega^2\bar{\mathbf{M}}\right]\mathbf{Q} = \mathbf{0}. \tag{9}$$

The discretized eigenvalue problem shows that the density and elastic modulus can be combined to a single input parameter for the SAFE analysis. Thus the dimensions of the parameters for investigating material and geometric properties are reduced by one dimension. The relationship between ρ and E in equation (9) can be substituted with the equivalent speed of sound, c, where $c^2 = E/\rho$. The discretized eigenvalue problem is then re-written as:

$$\left[\bar{\mathbf{K}}_1 + i\kappa\bar{\mathbf{K}}_2 + \kappa^2\bar{\mathbf{K}}_3 - \frac{\omega^2}{c^2}\bar{\mathbf{M}}\right]\mathbf{Q} = \mathbf{0}. \tag{10}$$

For a given material, equation (10) can be solved by either selecting the wavenumber, κ, and solving for the frequency, ω, or by selecting a frequency and solving for the wavenumber. In the latter case were ω is specified, the discretized equation (10) shows that the frequency, ω and the speed of sound, c, may be reduced to a single parameter, β, which is given by the ratio of the input frequency and speed of sound,

$$\beta = \frac{\omega}{c}. \tag{11}$$

The discretized eigenvalue problem in equation (10) can therefore be written as:

$$\left[\bar{\mathbf{K}}_1 + i\kappa\bar{\mathbf{K}}_2 + \kappa^2\bar{\mathbf{K}}_3 - \beta^2\bar{\mathbf{M}}\right]\mathbf{Q} = \mathbf{0}. \tag{12}$$

The group velocity relation in equation (5) can similarly be rewritten as

$$v_g = c\frac{\mathbf{Q}^T\left(\bar{\mathbf{K}}_2 + 2\kappa\bar{\mathbf{K}}_3\right)\mathbf{Q}}{2\beta\mathbf{Q}^T\bar{\mathbf{M}}\mathbf{Q}}. \tag{13}$$

The important implication of equations (12) and (13) is that if $\beta = \omega/c$ is solved over a wide enough range, results for different material properties (with different E and ρ) can be generated without resolving the eigenvalue problem. Thus, these results (dispersion curves for different E and ρ or c) can be determined by scaling the already computed dispersion curves. This is true since β contains both ω and material parameters, $c^2 = E/\rho$.

2.3. Selection of geometric parameters

An inverse problem is to be solved to estimate the material and geometric properties of a rail, which when input to a SAFE model will produce dispersion characteristics that match experimental measurements. Using the SAFE method, many models with different combinations of input parameters can be solved. It is however, important to minimize the number of input parameters to be estimated in the inverse problem because many more forward problems will have to be computed when the number of input parameters increases. The geometric parameters selected for estimation must allow sufficient flexibility of the rail

profile so that geometries encountered in practice can be described, and computed group velocities should be sensitive to changes of these parameters.

Many investigations on rail wear evolution have been published. Most of the work focuses on the wheel to rail contact problem. The investigations usually employ finite element modelling to simulate the rail vehicle dynamics and predict gradual wear of the rail. The wear behaviour is non-linear and dependent on factors such as the type of rail profile, curvature of the track, wheel profile and loading [10, 11, 12, 13]. The primary focus of our investigation is to estimate the current profile of the rail instead of profile prediction from simulation models. This investigation is limited to continuously welded rail with uniform cross-section. Non-prismatic sections such as switch rail sections discussed in [16] are not considered. Furthermore material properties are considered constant across the cross-section, and any non-linear effects of tension on the wave propagation are assumed to be captured in the range of allowable linear properties. Some authors [17] show that the head of the rail can be plastically deformed during the evolution of wear. Such effects are neglected.

It was realized that the major components of rail head geometry change are material movement, head height reduction and increasing convexity of the head. Material movement is seen when the interior of the rail head (which is in contact with wheel) is under stress and the exterior is not, therefore rail head material is plastically deformed and moves to the exterior of the rail. Head height reduction occurs when material on the rail head is constantly sheared from the top.

Various combinations of dimensions were investigated for representing realistic worn rail profiles. It was found that at least three dimensions are required to describe these wear characteristics and allow flexibility of the possible rail head geometries. The three dimensions of the UIC60 rail shown in red in Figure 3 were found to provide the best control over the rail geometry. Geometric parameters X_1, X_2 and X_3 enable a reduction in the head height, increased interior radius and a shaper exterior radius respectively.
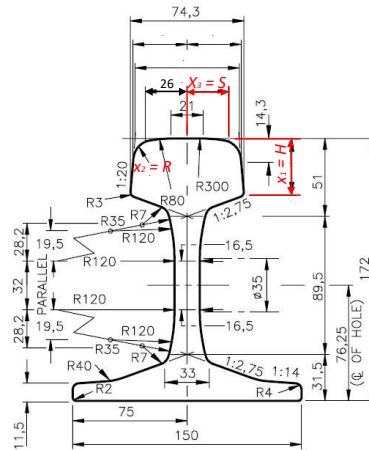

Figure 3: Standard UIC60 rail profile highlighting parameters used to describe a worn rail.

Adaptation of the rail mesh without user intervention is required for the process to be automated. A mesh movement strategy that avoids distortion of elements was adopted.

7

Parametric equations are used to define the head profile and boundary points of the rail profile. These parametric equations are solved for different input geometric parameters to create desired/worn profiles of the rail. The process then uses interpolation based on radial basis functions to move the internal nodes of the original mesh to new positions within the worn profile without excessive distortion of elements. The interpolation is controlled by the boundary nodes of the original and worn mesh.

The mesh moving algorithm based on radial basis function (RBF) interpolation [18] allows point-by-point mesh displacement interpolation of internal nodes from the displacement of boundary nodes. This process prevents distortion of the boundary elements by movement of internal nodes and eliminates the need to re-mesh the profile.

The process is illustrated in Figure 4. Figure 4a shows the original UIC60 rail profile and the worn rail profile that has to be meshed. The mesh of the worn profile without mesh movement and with mesh movement, are shown in Figure 4b and c. The worn rail mesh without mesh movement, shown in Figure 4b clearly shows that the mesh is distorted when the head boundary is displaced downwards, with some elements becoming inverted. Inspection of the worn rail mesh with mesh movement in Figure 4c shows that the nodes near the worn boundary move further than those further from the worn boundary. The meshes show that distortion of the mesh boundary elements is avoided when mesh movement is employed.

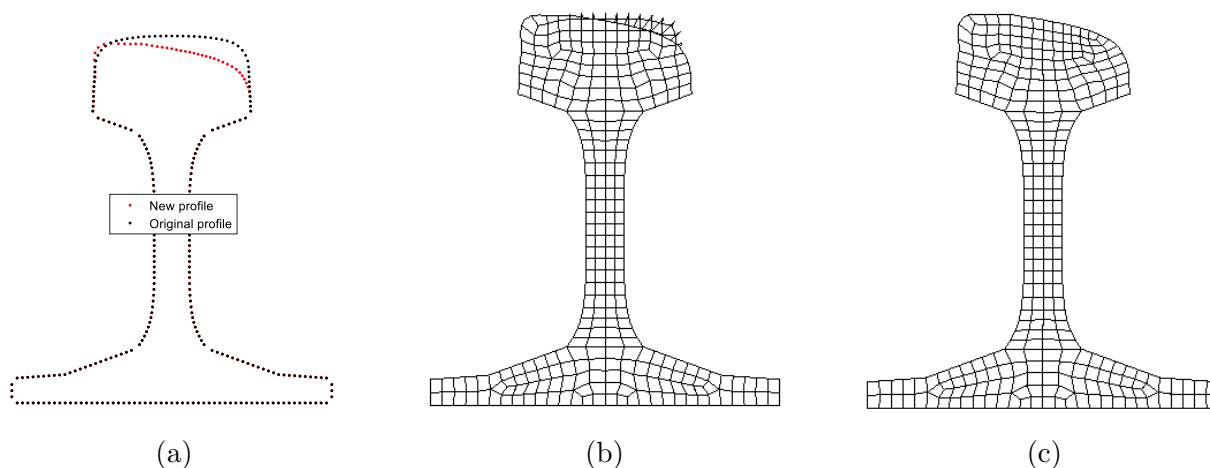|		
(a)	(b)	(c)

Figure 4: Illustration of mesh movement on a worn rail (a) Original and worn (new) boundary profile nodes. (b) Worn rail mesh without mesh movement illustrating element inversion. (c) Worn rail mesh after applying mesh movement.

2.4. Mode shape tracking

The SAFE method computes the wavenumbers at selected frequencies and a method was required to connect the discrete wavenumber - frequency points to form continuous curves. Loveday et al. [19] showed that for a symmetric rail profile the wavenumber-frequency curves of symmetric and antisymmetric modes cross each other while modes within the symmetric and antisymmetric families repel each other and do not cross. In the more

general case of an asymmetric rail profile the wavenumber-frequency curves do not cross and it is simple to track the modes. These curves may approach each other and then repel. In the repulsion regions the group velocities and mode shapes of the two modes swop. When comparing wavenumber frequency curves computed from different SAFE models the order of the modes may be different if the models are sufficiently different. A method for automatically identifying selected modes computed from any model and at any frequency is therefore required.

The foot of the rail is clamped to polymer pads on concrete sleepers and these pads damp energy in the foot of the rail. Modes with significant energy in the foot of the rail have very high attenuation and are not suitable for long range testing. There are however, a few modes that have little energy in the foot of the rail over certain frequency ranges and propagation over large distances can be achieved with these modes. Modes that have significant energy in the head of the rail are expected to be sensitive to changes in the geometry of the rail head and are suitable for estimating the geometry of worn rail. If such a mode is involved in mode repulsion, the mode shapes swop and the second mode becomes suitable for estimating the geometry of worn rail after the repulsion. Therefore, when trying to focus on a mode that propagates long distances in the field it is more appropriate to track the mode shape in the SAFE computed results. Three mode shapes that propagate long distances, which are excited and sensed with transducers mounted under the head of the rail, have been identified.

A tracking technique was implemented to track these three mode shapes using preselected samples of these mode shapes. The modal assurance criterion (MAC) [20], which performs correlation of mode shapes, was used to detect the three head mode shapes in all the computed mode shapes from the SAFE models with different input parameters. A correlation, ranging from 0 to 1, is computed using the reference and computed mode shapes. Values closer to 0 indicate that mode shapes are not similar while values closer to 1 indicate similarity between the compared mode shapes. The formula for MAC proposed by Ting et al. [20] is given as:

$$MAC(\Phi_{Ai}, \Phi_{Xj}) = \frac{|\{\Phi_A\}_i^T \{\Phi_X\}_j|^2}{\{\Phi_A\}_i^T \{\Phi_A\}_i \{\Phi_X\}_j^T \{\Phi_X\}_j} \qquad (14)$$

where, Φ_{Ai} and Φ_{Xj} are the i and j^{th} eigenvectors of the reference and extracted mode shapes.

Three groups of reference mode shapes were created by manually selecting head mode shapes in the frequency range of 35 kHz to 42 kHz at twenty equally spaced interval points from the solution of a SAFE model of the unworn UIC60 rail. These frequency limits were chosen according to the operating frequency range of transducers used for field measurements. For each reference group, four samples of the manually selected mode shapes are shown in Figure 5. The head mode shapes are expected to combine with other mode shapes near repulsion points. Two of the Group 3 mode shape samples in Figure 5 show motion in the entire cross-section of the rail, thus indicating that the samples were taken near repulsion points.
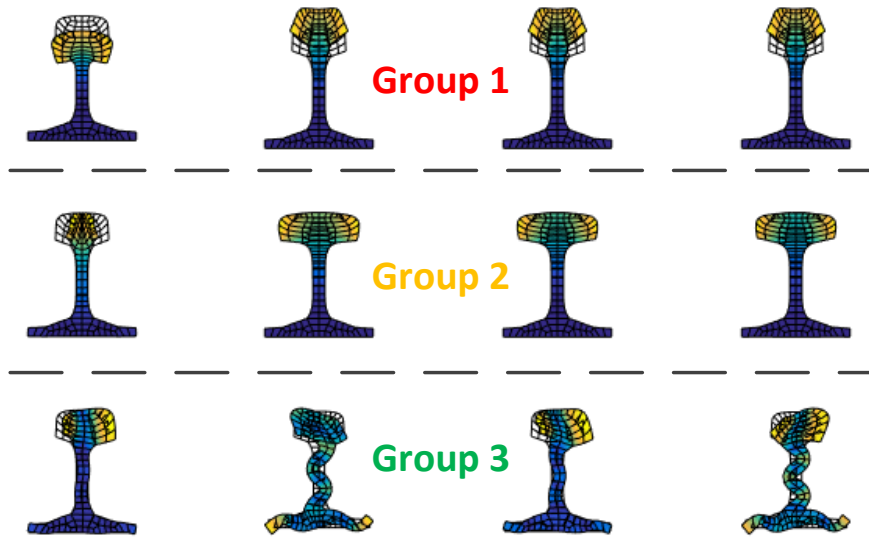
Figure 5: Examples of mode shapes for each group manually selected at different frequencies.

When new mode shapes were computed, from a SAFE model with different input parameters, these mode shapes were correlated with all the mode shapes in the reference groups. The new mode shape that had the highest sum of correlation values for each group is selected as the mode shape belonging to that group. This assumes that a mode shape that corresponds with each group propagates at the frequency of interest and can therefore be selected. The diagram in Figure 6 shows an illustration of the process.
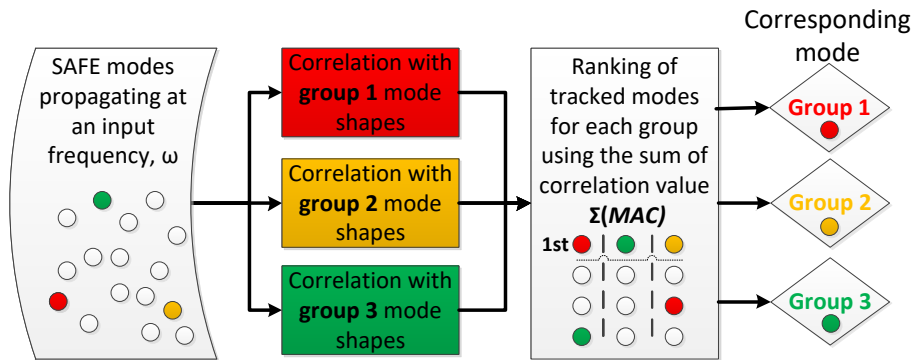

Figure 6: Illustration of the mode shape tracking process using selected mode shape groups.

Figure 7 shows wavenumber and group velocity points computed from a SAFE model of a worn rail. The mode shape tracking technique was used to select the points belonging to the three reference mode shape groups and coloured curves are drawn through these points. The dispersion curves are named Group 1, Group 2 and Group 3 for the convenience of referring to these curves in this paper. Dispersion curves of the Group 3 mode shapes (highlighted in

10

green) are only extracted for group velocities greater than the group velocities of the Group 1 mode shapes (highlighted in red). Inspection of the mode shapes at selected dispersion points showed that the correct mode shapes were selected to form the dispersion curves. It must be noted that the dispersion curve for the Group 3 mode shape is in fact made up of three segments of wavenumber-frequency dispersion curves which have similar mode shapes. The corresponding three segments are clear in the group velocity plots which also show rapid changes in the group velocity in the mode repulsion regions between the line segments.
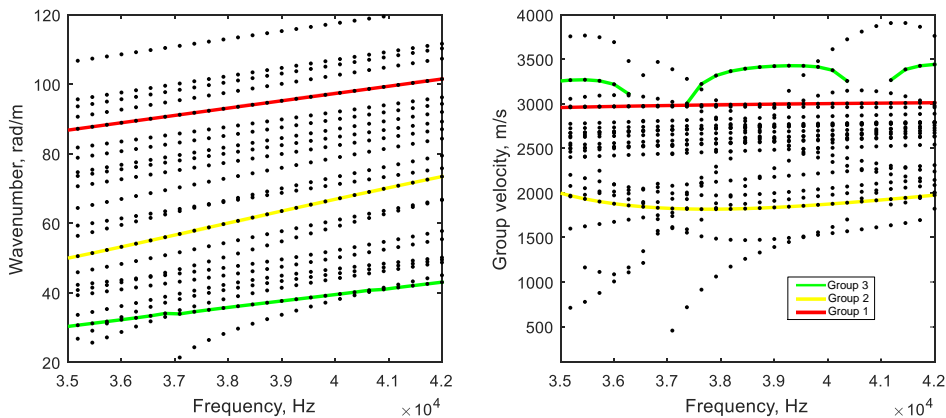

Figure 7: Extracted dispersion curves for identified mode groups.

3. Procedure for estimating rail properties

The aim of this paper is to estimate rail material and geometric properties from experimental measurements. Specifically, the material properties of interest are the speed of sound $(c = \sqrt{\frac{E}{\rho}})$ and the Poisson's ratio (ν), while the geometric parameters being sought include S, R and H as depicted in Figure 3. The measurements capture reflections from aluminothermic welds at unknown distances from the transducer using a pulse-echo mode of operation. The time domain measurements can be represented in the time-frequency domain as spectrograms which, due to dispersion, contain frequency-dependant bands of energy corresponding to the times of arrival of reflections from welds. The objective is therefore to solve the inverse problem of finding rail material and geometric parameters that, when used as input parameters in a SAFE model, reproduce the measured dispersion characteristics as accurately as possible. This section describes the proposed procedure.

3.1. Signal processing of experimental data

Figure 8 illustrates the relationship between the spectrogram and the group velocity curve for a single mode of propagation. The top right of Figure 8 shows a typical group velocity curve $v_g(\omega)$ of a dispersive mode plotted with group velocity on the horizontal axis and frequency on the vertical. This group velocity dispersion curve is used to propagate a Hanning-windowed tone-burst a known distance $2D_w$, corresponding to a round trip distance

11

to a weld a distance D_w from the transducer and back. The signal that the transducer would receive in this case is depicted in the top left of Figure 8. The figure below the time signal on the left represents a spectrogram of the time signal computed using a Short-Time Fourier Transform (STFT) [21]. The group velocity curve on the right can similarly be transformed to a time-frequency curve representing the frequency-dependent times of arrival of a reflection at a distance D_w from the transducer using the expression

$$T(\omega) = \frac{2D_w}{v_g(\omega)}. \tag{15}$$

These two time-frequency representations are overlaid in the figure at the bottom of Figure 8. Since this distance to the weld D_w is generally not known, a technique that does not explicitly require knowledge of the distance is proposed in this section.
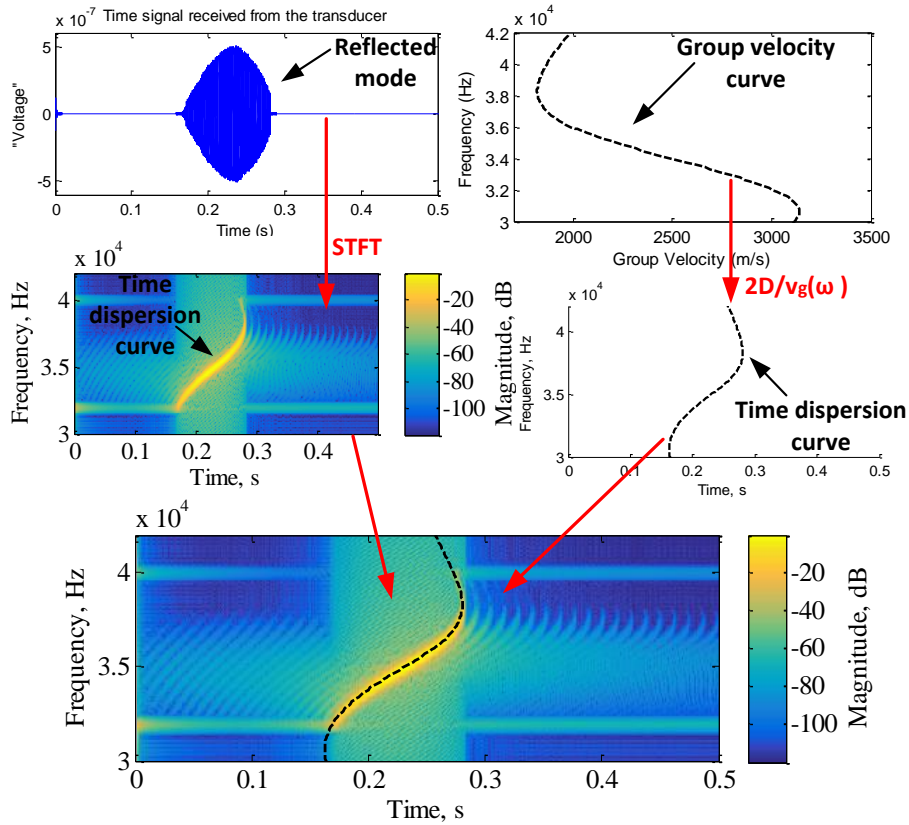

Figure 8: Illustration of the generation of equivalent time dispersion curves of a reflected mode: one using a time signal and STFT, the other calculated using the group velocity curve and weld distance.

Examples of two different experimental time signals captured in the field are depicted in Figure 9. The measurements were performed using two different transducers, each of which preferentially excite different modes of propagation in the rail. The measurements were also performed some days apart and at different times of day. Two different measurements are used to evaluate the robustness of the proposed property estimation procedure. The

12

first measurement shown in Figure 9a, was performed using a transducer that preferentially excites the Group 1 (non-dispersive) mode shapes. The second measurement depicted in Figure 9b was performed using a transducer that excites the Group 3 (fast-dispersive) mode shapes more strongly.

A Short-Time Fourier Transform (STFT) [21] can be used to convert the two measured time signals to the time-frequency domain, and the results are depicted as the spectrograms Figure 10. The spectrogram in the time-frequency domain will be denoted $\mathbf{S}(t, \omega)$. Figure 10a is computed using the time signal shown in Figure 9a, while Figure 10b is generated using the time signal depicted in Figure 9b. The bands of energy on the spectrograms in Figure 10 represent the times of arrival of different modes of propagation, reflected from different welds in the rail.

Some of the most pronounced reflections are highlighted in Figure 10. In order to relate reflections on the spectrogram to mode groups, the following notation is introduced: uncoupled reflections from a specific weld will be denoted as $\alpha(n, n)$, where α represents the weld position, as illustrated in Figure 1, and where n represents the mode group as defined in Figures 6 and 7. Coupled reflections due to mode conversion [22] will similarly be referred to as $\alpha(n, m)$, where n and m are two different mode groups resulting from scattering or mode conversion at the weld. So, for example the reflection of mode group 1 incident and mode group 3 reflected from weld b would be denoted $b(1, 3)$. It should be noted that for coupled modes, n and m are interchangeable since the time of arrival of $b(m, n)$ would be identical to $b(n, m)$.

Uncoupled reflections $\alpha(1, 1)$ and $\alpha(3, 3)$ as well as coupled reflection $\alpha(1, 2)$ appear most prominently in Figure 10a, with the reflections from welds c and d highlighted for example in the figure. The same modes are apparent in Figure 10b. The non-dispersive mode (Group 1) is clearly more strongly excited in the results presented in Figure 10a than Figure 10b due to the fact that different transducers are used as previously stated. Figure 10a also shows how, due to the very different group velocities of the different modes, it is possible for reflections from more distant welds to overlap with reflections from welds closer to the transducer, thereby complicating the processing.
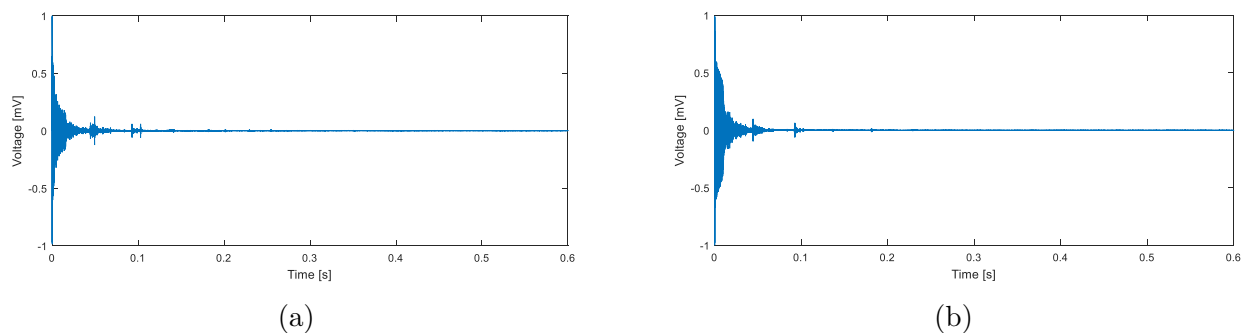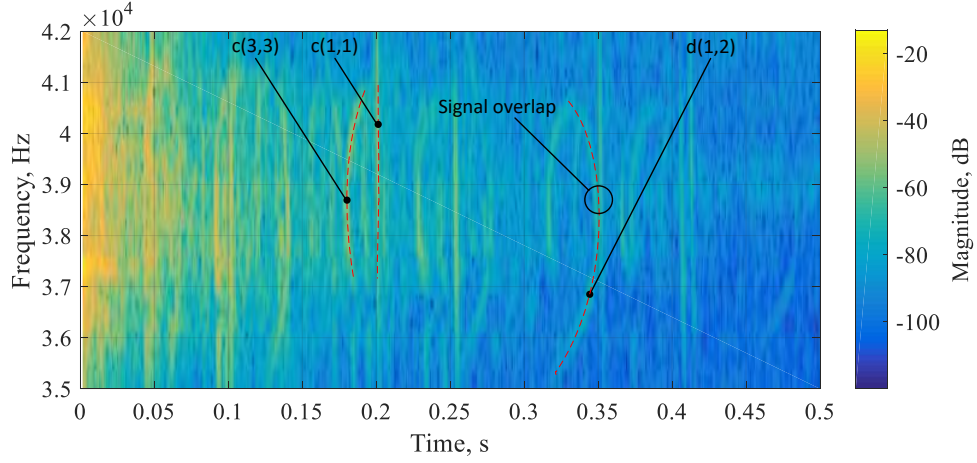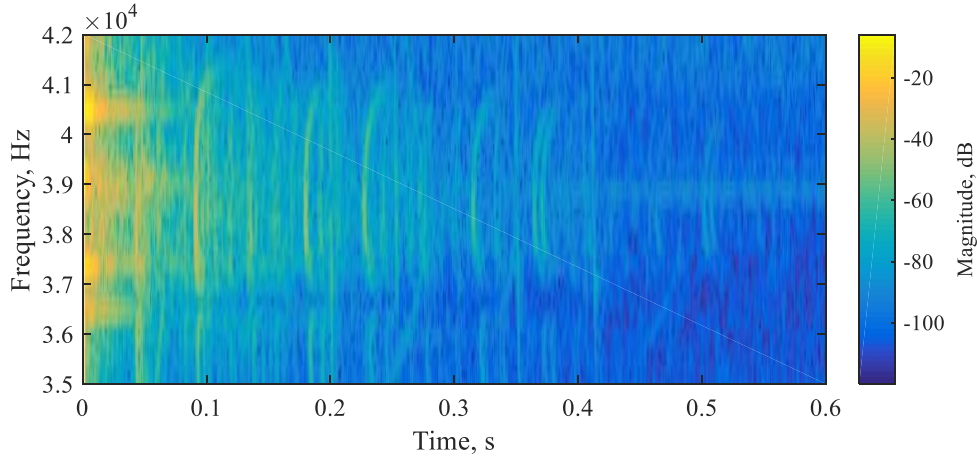

(a)   (b)

Figure 9: Pulse-echo measurements performed using two different transducers on a UIC60 rail (a) Measurement 1. (b) Measurement 2.

13

Figure 10: (a) Spectrogram of the first pulse-echo measurement conducted on a UIC60 rail showing the coupled and uncoupled head mode reflections. (b) Spectrogram of the second pulse-echo measurement

In order to overcome the challenge of not knowing the distances to the welds *a priori*, a method is required to relate the frequency-dependent times of arrival of reflections, to the weld distances. The proposed method exploits the relationship presented in equation (15) written in terms of round trip distance $2D_w$ and the fact that the distance to a given weld must be constant for each frequency and for each mode received.

As illustrated in Figure 11 for a single mode, if the correct group velocity curve is used for the transformation, the result will be a vertical line at the distance $2D_w$ corresponding to the round-trip distance to the weld. When multiple dispersive modes are considered, as is the case with our experimental measurements, only a SAFE model which accurately represents the material properties and geometry of the rail will correctly predict the group velocity for each mode. If an inaccurate SAFE model is used to predict the distances, a slightly different

14

round-trip distance will be predicted at each frequency, i.e.:

$$2D_w(\omega_i) = T(\omega_i)v_g(\omega_i), \ i = 1, 2, ..., n_f, \tag{16}$$

where n_f are the number of discrete frequency points considered.

For each mode and at each frequency the spectrogram in the time-frequency domain can similarly be transformed to a spectrogram in the distance-frequency domain through a multiplication by the frequency-dependent group velocity curve, as:

$$\mathbf{S}(d, \omega_i) = \mathbf{S}(t \cdot v_g(\omega_i), \omega_i), \ i = 1, 2, ..., n_f, \tag{17}$$

where $\mathbf{S}(d, \omega)$ represents the spectrogram transformed to the distance-frequency domain.
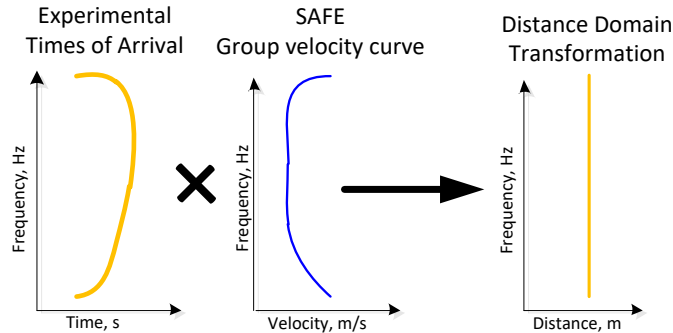

Figure 11: Illustration of how arrival times can be transformed using the correct group velocity curve. The symbol: $\times$ is used to show element-wise multiplication.

3.2. Latin hypercube sampling

A simple exhaustive search strategy is employed to determine the material and geometric properties which, when used as inputs to the SAFE model, result in the best agreement with the measured dispersion properties as represented in the spectrograms in Figure 10. Other, more sophisticated search or optimization methods could also have be used to search the parameter space (for example in [15] a pan-and-zoom method was employed) but these would require introducing new samples and re-solving the SAFE eigenvalue problem in equation (12) to compute group velocity curves. The method proposed here makes use of a database of group velocity curves which can be pre-solved and stored. It is therefore not necessary to re-solve the SAFE eigenvalue problem as long as the sampled SAFE solutions are able to represent the actual geometry and material properties of the physical rail.

Latin Hypercube Sampling (LHS) [23] is used to uniformly sample the space of possible geometrical and material parameters. A total of 4,000 samples are generated using the `lhsdesign` function in Matlab for the following four parameters: $27.5 \leq H \leq 37.5$, $26 \leq S \leq 36$, $13 \leq R \leq 21 \ mm$ and $0.25 \leq \nu \leq 0.35$. Selected points in the sample space are illustrated graphically in Figure 12. The figure presents the sample points in terms of their deviation from the original UIC60 rail profile, so for example ΔH is the change in height from the unworn rail profile. For each of these sampled points, the eigenvalue problem in

15

equation (11) is solved over sufficiently wide range of β so that another 40 samples of different speeds of sound $4,800 \leq c \leq 5,200 \; m/s$ can be generated using the scaling presented in equation (13). In total therefore, $4,000 \times 40 = 160,000$ sets of group velocity curves are compared to the experimental spectrograms, although only 4,000 SAFE models are required to be solved and the resultant group velocities stored. In Section 3.3 the method used to determine which group velocity curves best fit the experimental measurements is presented.
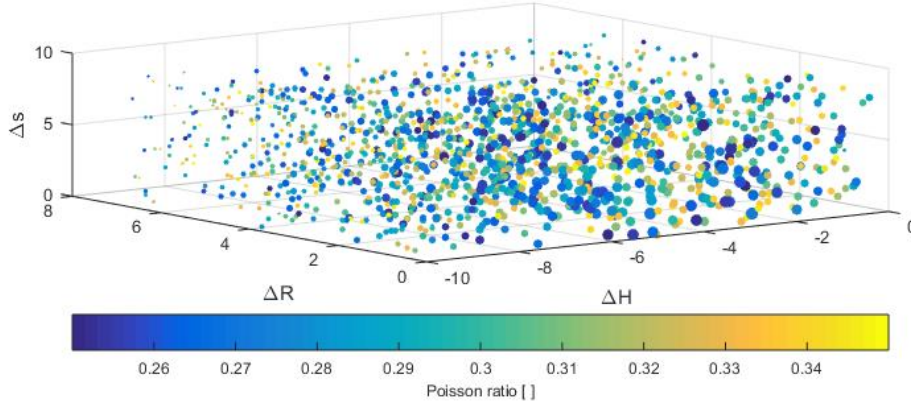

Figure 12: Sampled parameter space using 4,000 LHS samples over the upper and lower bounds of geometric parameters and Poisson's ratio.

3.3. Procedure for estimating properties

In the previous section, the method used to generate candidate SAFE models with geometric and material properties sampled within a specified sample space is presented. Each of these SAFE models result in a unique set of group velocity dispersion curves. From these dispersion curves, the three modes known to propagate along the rail with low attenuation were identified, as described in Section 2.4. In this section, the method used to evaluate how closely these group velocity dispersion curves fit the experimental measurements is presented. In order to compare the results, the distances to the welds are also required and since this information is not known *a priori* the weld distances are also to be inferred during the proposed procedure.

The process starts by computing the dispersion curves for modes of interest for each sample point over a range of β values. The range of β is chosen such that the scaling presented in equations (11) and (13) can be used to generate group velocity-frequency dispersion curves in a wide enough frequency range, with speed of sound in the range ($4800 \leq c = \sqrt{\frac{E}{\rho}} \leq 5800 \; m/s$). In total, for each LHC sample point, dispersion curves for 40 evenly spaced c values are computed. All three uncoupled modes depicted in Figure 7 as well as the three possible coupled modes (Groups (1,2), (1,3) and (2,3)) are considered. (Recall that the time of arrival curves for the coupled modes are given by the average of the two constitutive modes; or equivalently the apparent group velocity is the average of the two constitutive group velocities.) In total therefore, for each candidate solution H_i, R_i, S_i, ν_i and c_{ij} (where

16

j represents one of the 40 evenly spaced c samples for each sample of i); a total of six group velocity curves are computed, namely the three uncoupled and the three coupled group velocity curves.

The next step in the process is to use the 6 computed group velocity curves to transform the spectrogram from the time-frequency to the distance-frequency domain, as illustrated in Figure 11, and detailed in equation (17). In this case, six transformed spectrograms are computed for each candidate solution, one for each group velocity curve used in the transformation. Next, these transformed distance-frequency spectrograms are combined using a simple summation:

$$\mathbf{S}_{total}(d, \omega) = \sum_{i=1}^{6} \mathbf{S}_i(d, \omega), \tag{18}$$

where $\mathbf{S}_i(d, \omega)$ is a matrix representing the distance-frequency spectrogram. It should be noted that the transformed spectrograms no longer have a regular distance spacing due to the transformation and therefore some interpolation is require to perform the summation. Examples of these combined frequency-distance spectrograms are shown in Figures 14.

If the group velocities used to transform the spectrogram to the distance domain are similar to the group velocities of the modes in reality, firstly dispersive times of arrival will be straightened and will all correspond to the actual distance to the welds. Furthermore, each mode will similarly be straight and all modes will have a vertical arrival indicators at the same distance. If the group velocities used in the transformation do not closely match the group velocities of the physical rail, the energy will be spread over a range of distances. Therefore, the combined frequency-distance spectrograms are summed at each frequency using

$$B(d) = \sum_{i=1}^{n_f} \mathbf{S}_{total}(d, \omega_i), \tag{19}$$

where n_f is the total number of frequency points and where $B(d)$ is a curve which should have local maxima at the locations of the welds.

Figure 13 shows examples of what we would expect $B(d)$ to look like if a model which closely resembles the physical rail is used, as well as one which does not. The local maxima (peaks) at weld distances are far more pronounced for the good model than for the poor model. Therefore, the peak prominences can be used as a measure of how well the inputs into the SAFE model fit the physical rail characteristics. The Matlab function `findpeaks` is employed to find the most prominent peaks [24], which can be written as $P_i(B(d))$, $i = 1, 2, ...$ where i represents the ith most prominent peak. Figure 13 highlights $i = 1, 2, 3$ most prominent peaks and indicates their peak prominence $P_i(B(d))$ which is essentially a measure of the height of the peak.
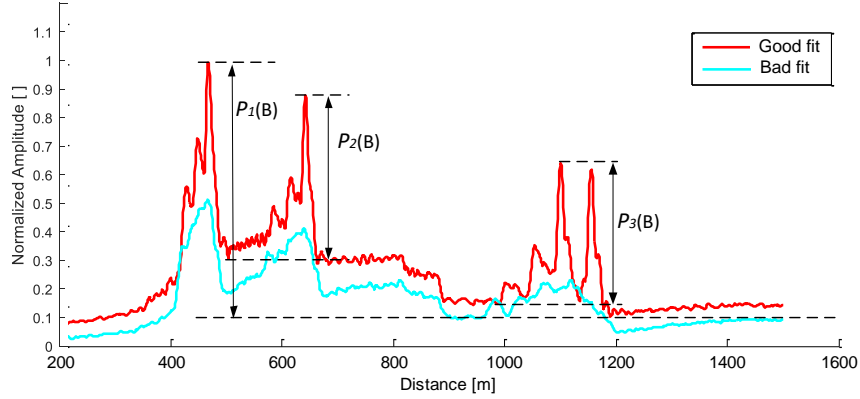
Figure 13: Illustration of $B(d)$ for a good and a poor SAFE model, with higher peak prominence $P_i(B(d))$ when an accurate SAFE model is used.

Lastly, the peak prominences can be sorted and a measure of how well a particular sample point fits the physical rail characteristics can be defined by summing a selected number of the highest peak prominences. The selected number of peak prominences or weld locations to measure is dependent on the monitoring distance. The transducers used for this study could detect at least six weld reflections within a kilometer distance from the transducer. It should be noted that the extracted peaks with highest prominences are automatically identified by the algorithm and therefore only the number of peaks to search for is required. The measure of fit for each SAFE model is therefore computed as

$$P_{total} = \sum_{i=1}^{m} P_i(B(d)) \tag{20}$$

where m is the selected number of weld reflections to be used to estimate the rail properties. In Figure 12 the measure of fit for each sample is represented by the size of the sphere.

4. Results and discussion

The procedure described in Section 3.3 is evaluated in this section, using the two pulse-echo measurements conducted on the UIC60 rail, and with respective spectrograms presented in Figure 10. The settings used for the Latin Hypercube Sampling are as detailed in Section 3.2. In order to test the procedure, the five most prominent weld reflections are considered, and therefore $m = 5$ is used in equation (20).

4.1. Transformed spectrograms and measures of fit

The proposed measure of fit given in equation (20) is computed for each of the 160,000 samples, for the two spectrograms depicted in Figure 10. Models with the best fit (highest value of P_{total}) and worst fit (lowest value of P_{total}) are noted for each measurement. It is expected that the models which best fit the measured results will be slightly different, especially the speed of sound c, since the elastic modulus is known to be sensitive to temperature [9]) and the two measurements were performed at different temperatures.

18

Figure 14 depicts the spectrograms computed after the transformation using the six group velocity curves computed for the best and worst sample point respectively, and after the summation as described in equation (18). Figure 14a and 14b depict the results using the measured spectrograms in Figure 10a and 10b respectively, transformed using the best SAFE model; while Figure 14c and 14d present the same results for the worst SAFE model.

The results in Figure 14a and 14b have pronounced energy bands corresponding to the weld distances (which are also indicated on the figures). However, energy bands depicted in Figure 14c and 14d computed using the worst SAFE models are far less prominent.

The transformed spectrograms in Figure 14 are summed at each frequency, as described in equation (19) and the results are depicted in Figure 15. In this case, both the results for the best and worst fits are depicted. The worst model shows less prominent peaks compare to the best model, and therefore since the peak prominence is lower, the corresponding measure of fit, given in equation (20) is also lower. Distances to the welds as approximately measured in the field are also indicated in the figures and correspond to the peaks of the $B(d)$ curves. The most prominent peaks represent the distances to the welds extracted by the proposed procedure.
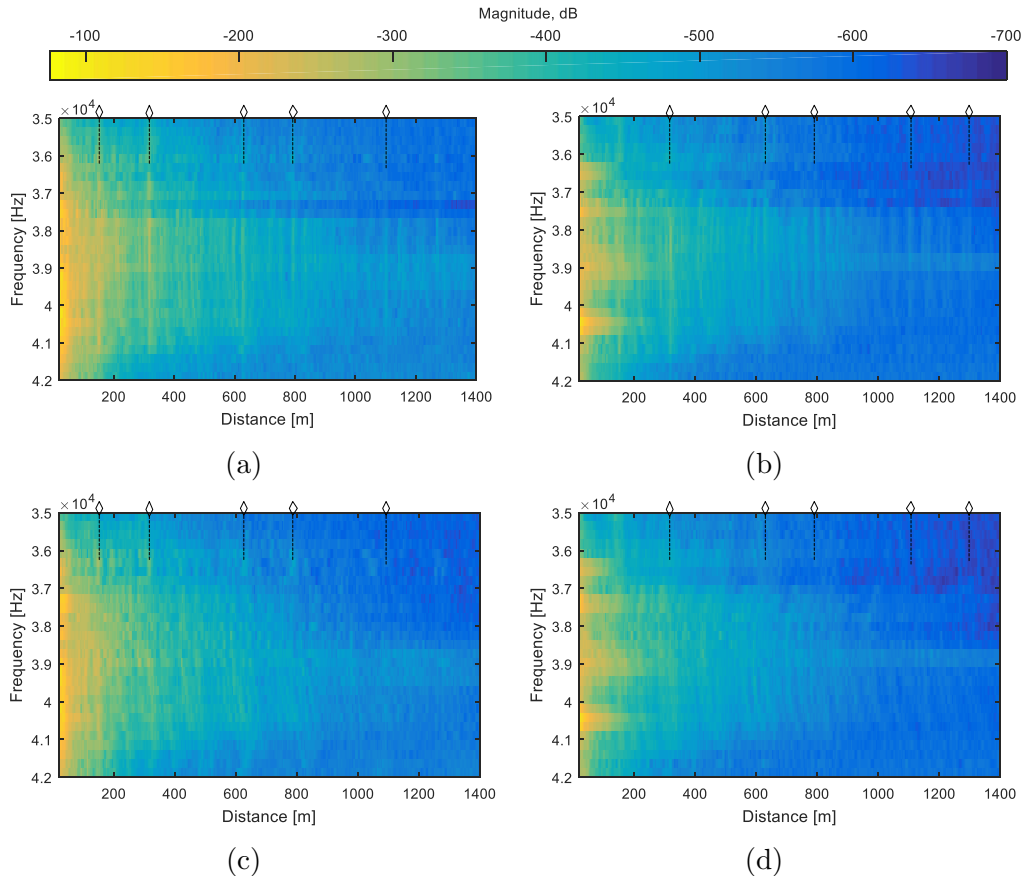

Figure 14: Summed distance-frequency spectrograms, $\mathbf{S}_{total}(d,\omega)$ created using the best and worst SAFE models. (a) Measurement 1: Best model. (b) Measurement 2: Best model. (c) Measurement 1: Worst model. (d) Measurement 2: Worst model.
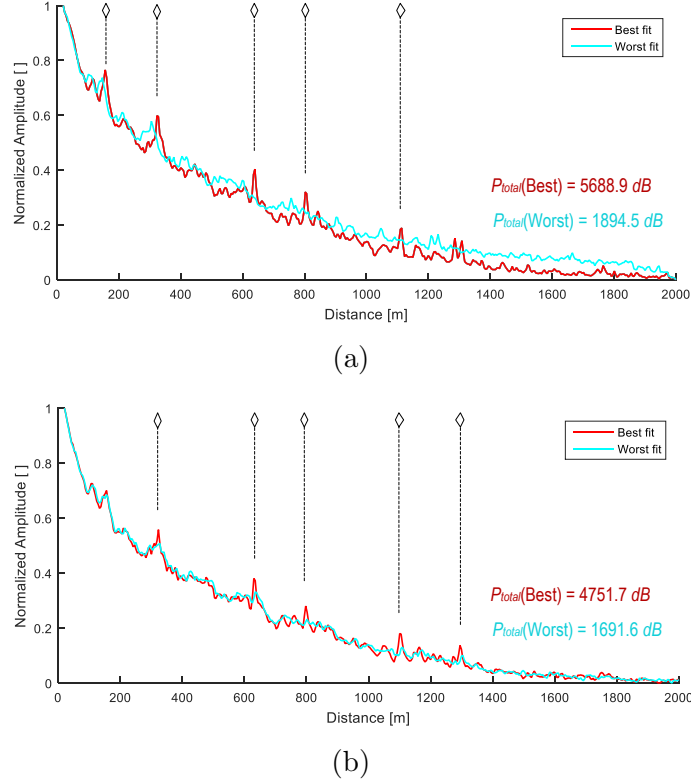
19

Figure 15: $B(d)$ for the best and worst models. (a) Measurement 1. (b) Measurement 2.

The distances to the five most prominent welds, which correspond to the peaks in Figure 15a and 15b are presented in Table 1. Good agreement between the two sets of results is achieved. For the first measurement, the five most prominent peaks correspond to the 5 welds closest to the transducer, but for the second measurement a more distant weld (labeled f in Table 1) has a more prominent peak than the closest weld (a). Figure 15b illustrates that the peak for this closest weld (a) is present in the $B(d)$ curve, and if more peaks were used to compute the measure of fit, this closest weld would have been detected. The prominence of the individual peaks is also presented in Table 1. The peak prominences for the two measurements tend to reduce with an increase in distance to the welds due to the attenuation. However, the prominence of weld (a) is relatively low due to the large coherent noise in the first part of the time signal as depicted in Figure 9.

The predicted distances, together with the group velocities for best fit models are used to generate time of arrival curves (see equation (15)) and superimposed on the measured spectrograms, illustrated in Figure 10. These results are depicted in Figure 16, with the six predicted times of arrival for each weld separately highlighted. The significantly different group velocities of the different modes results in overlapping of the times of arrival for different welds, especially between 0.3 and 0.4 seconds. The proposed procedure overcomes this complexity and achieves very good agreement between the predicted time of arrival curves using the best fit models and the experimental measurements.

20
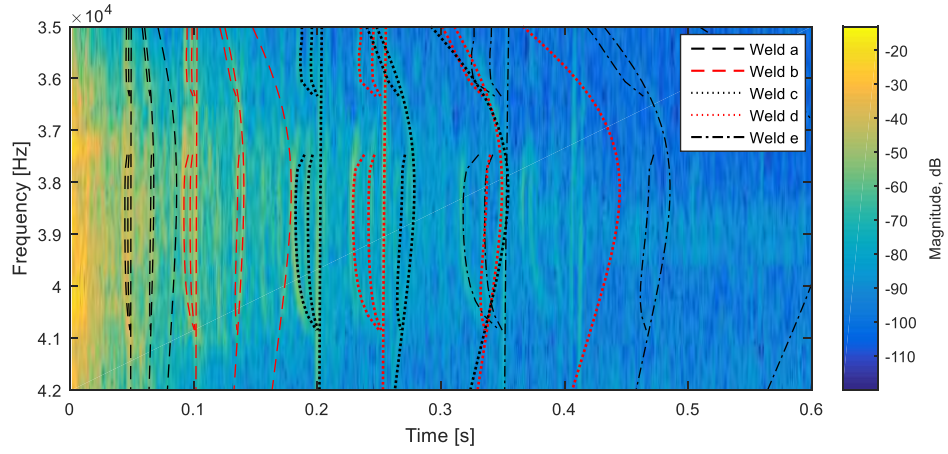
(a)
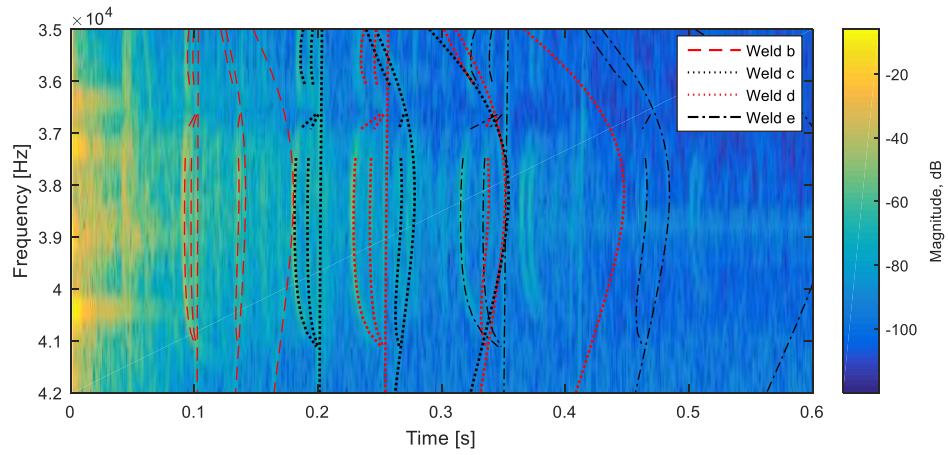
(b)

Figure 16: Estimated arrival time curves superimposed on spectrograms computed using field measurements. (a) Measurement 1. (b) Measurement 2.

Table 1: Aluminothermic weld distance estimates, and associated peak prominence, using the proposed procedure.

Aluminothermic weld	a	b	c	d	e	f
Measurement 1 distances [m]	77.81	161.45	315.14	398.77	550.21	-
Measurement 2 distances [m]	-	161.44	317.40	398.76	552.46	649.66
Prominences: measurement 1 [ ]	906.9	1576.8	1240.3	1136.1	828.9	-
Prominences: measurement 2 [ ]	-	1273.0	1033.3	987.0	769.1	689.2

4.2. Estimated rail properties

Finally, a comparison between measurements of the physical rail geometry in the field and geometrical parameters extracted using the proposed process are presented in Table 2. The

geometry was measured at only one location close to the transducer attachment point, but this geometry is considered representative of the average geometry of the rail in the section where the measurements were preformed. It should also be noted that the process used to measure the geometry is not very accurate [15] (typically accuracy in the order of 0.5mm is expected). The results presented in Table 2 demonstrate that the geometry of the rail has been predicted to an acceptable degree of accuracy. The elastic modulus, which is related to the speed of sound, is known to change with temperature [9]. Therefore, the slight variation in the speed of sound in the rail can be as a result of the difference in temperature when the two measurements were conducted.

The consistency in the results presented in this section and the agreement with both spectral (see Figure 16) and physical profile measurements (see Table 2) indicates that the procedure developed in this study can accurately estimate properties of rails. The procedure also shows some robustness for measurements performed with different transducers which preferentially excite different modes of propagation in the rail.

Table 2: Comparison between the estimated parameters using the proposed procedure and physical geometry measurements

Geometric Variable	ΔH [mm]	ΔR [mm]	ΔS [mm]	ν	c [m/s]
Field Measurement	-2.4	0	+2	-	-
Measurement 1	-2.779	+0.194	+0.685	0.272	5107.7
Measurement 2	-2.633	+0.064	+1.797	0.266	5128.2

The estimated parameters from the models appear to be realistic but there could be models that produce a fit almost as good as the best model but have clearly incorrect parameters. This would indicate an inverse problem that is not well-posed and may produce poor estimates. In order to investigate if the problem is well-posed we further investigate the highest value of P_{total} for each of the 4000 LHS samples. For each sample or combination of parameters H_i, R_i, S_i, ν_i, c_{ij} the value P_{total} was computed for the $j = 1 : 40$ samples of the speed of sound, c_{ij}, and the highest value of P_{total} is denoted $P^*_{total i}$ while the speed of sound corresponding to $P^*_{total i}$. is denoted c^*_i. The highest value of P_{total} may then be found and denoted $\hat{P}^*_{total} = \max_i P^*_{total i}$ and the 4000 samples can be ranked according to the 4000 values of $P^*_{total i}$.

The distribution of the best samples within the sample space are then investigated by plotting the samples above a selected fraction or threshold of $\hat{P}^*_{total}$. The four plots in Figure 17 show all the samples, those samples above $0.7\hat{P}^*_{total}$, $0.8\hat{P}^*_{total}$ and $0.9\hat{P}^*_{total}$ respectively. The size of the markers in these plots is proportional to the value of $\hat{P}^*_{total i}$ for sample i and the smaller markers are therefore eliminated as the threshold is increased. The remaining volume,V_{rem}, of the LHS parameter space corresponding to increases in the threshold are also shown on the plots. V_{rem} is given as the percentage volume of the sampling space that remains for set thresholds compared to the original sampling space.The ranges of the speeds of sound, c^*, for the different thresholds are also shown in Figure 17.

The volume containing the samples decreased as the threshold is increased, indicating that

the better samples are distributed closer to the optimal sample in a single cluster. This indicates that the inverse problem is reasonably well-posed. Figure 17d shows that the parameter ranges reduce to $34.61 \leq H \leq 35.66$, $26.69 \leq S \leq 31.54$, $13.06 \leq R \leq 14.06$ mm, $0.254 \leq \nu \leq 0.272$ and $5066.67 \leq c^* \leq 5148.72 m/s$ for a 90% threshold. Figure 17 also indicates that the forward problem is least sensitive to S given the relatively large range relative to the other parameters. This large variance in S therefore suggests that it is the most difficult parameter to estimate in the inverse problem.
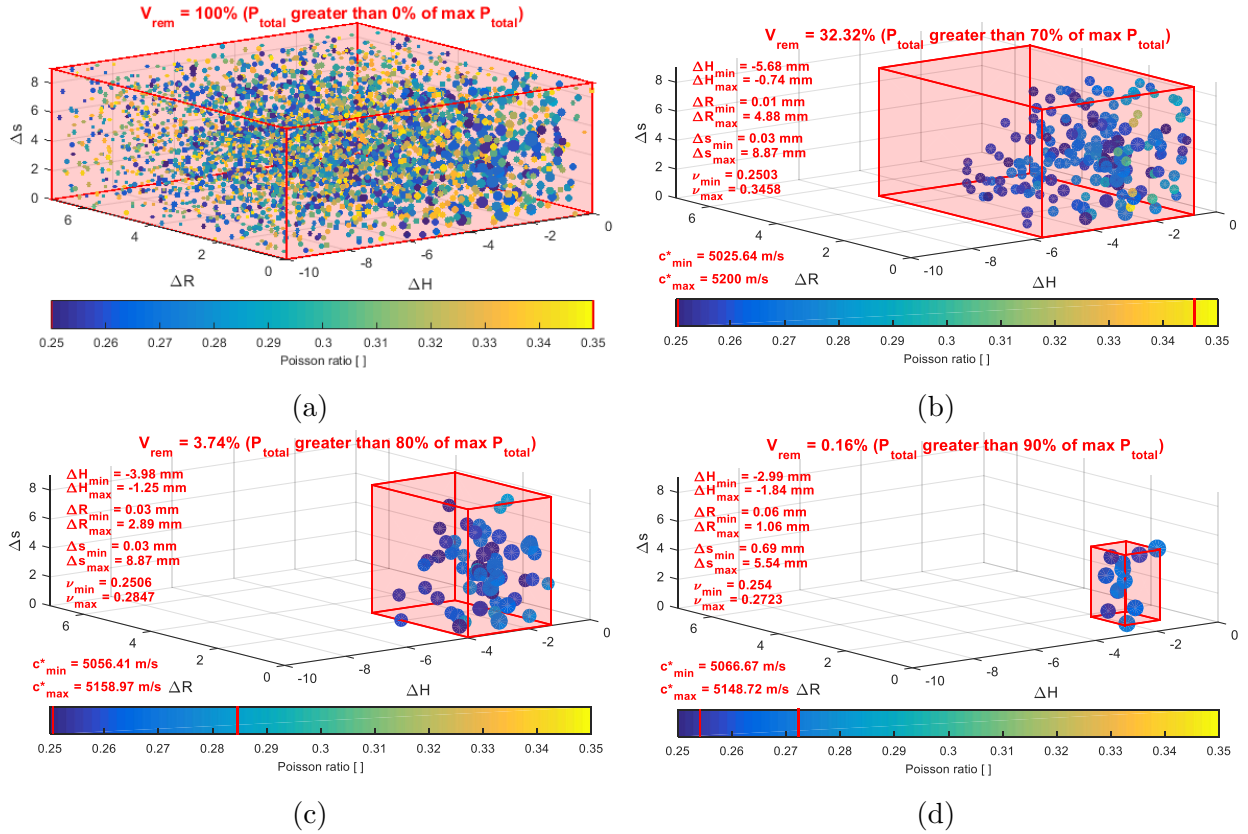

Figure 17: The highest measure of fit, P_{total}, for all LHS samples greater than (a) 0% of the maximum P_{total}. (b) 70%. (c) 80%. (d) 90%.

5. Conclusions

A procedure was developed to estimate material and geometric properties of a rail by finding the properties which, when input into a SAFE model, accurately reproduce measured dispersion characteristics. Analysis of the SAFE method matrices, for an elastic isotropic homogeneous rail, showed that the elastic modulus, density and frequency can be combined as one parameter in the eigenvalue problem. Therefore only a single set of dispersion curves needs to be calculated using the SAFE method for a particular Poisson's ratio and speed of sound with curves for other speeds of sound being obtained by simply scaling these curves.

It was found that the geometry of the rail head due to wear and grinding of can be represented by changing three selected geometric parameters. An automated procedure for adapting the finite element mesh to account for wear and grinding without causing element distortion was implemented. Experimental pulse-echo measurements with transducers attached under the head of the rail were used to determine dispersion characteristics. Various modes that propagate long distances were identified and the reflections of these modes from aluminothermic welds were observed in time-frequency spectrograms. A method for automatically identifying these particular modes in the modal predictions from the SAFE models, computed using different material and geometric properties of the rail, was developed by correlating the mode shapes with groups of manually identified mode shapes. Dispersion characteristics were computed for a total of 4,000 SAFE models with different combinations of Poisson's ratio and the three geometric parameters. For each of these models the dispersion curves were scaled to represent 40 different speeds of sound giving a total of 160,000 sets of dispersion curves. A technique was developed to identify which set of dispersion curves best fit the experimental spectrograms without using any knowledge of the distances to the reflectors. In addition to estimation of the rail properties, the procedure also estimated the distances to the aluminothermic welds. The technique was applied to two measurements performed with different transducers and on different days on the same section of rail. The estimated parameters for the two measurements were similar. The distances to the welds appear to be correct and the estimated rail geometries were similar to measurements of the rail geometry performed at one location. The dispersion curves and estimated distances from the best models were overlaid on the measured spectrograms and showed excellent agreement.

The estimation technique was developed specifically for this application and was only tested using the selected modes, the selected three geometric parameters and two measurements. The inverse problem appears to be well-posed for this specific case. It is suspected that dispersive modes are required for the technique to be effective. Further research should be performed to investigate what conditions are required for the technique to work or when the inverse problem becomes ill-posed.

The inverse problem was solved by simply finding the SAFE model that provided the best fit from a sample of possible models. The use of a response surface to interpolate the sample space should be investigated.

Acknowledgments

References

[1] X. Liu, R. Saat, C. P. L. Barkan, Analysis of causes of major train derailment and their effect on accident rates, Transportation Research Record: Journal of the Transportation Research Board 2289 (1) (2012) 154–163.

[2] F. Burger, P. Loveday, Ultrasonic broken rail detector and rail condition monitor technology, in: Proceedings of the 11th International Heavy Haul Association Conference (IHHA 2017), Cape Town, South Africa, 2017, pp. 275–280.

[3] P. Loveday, C. Long, Long range guided wave defect monitoring in rail track, in: AIP Conference Proceedings 1581, 2014, p. 179.

[4] L. Gavrić, Computation of propagative waves in free rail using a finite element technique, Journal of Sound and Vibration 185 (3) (1995) 531–543.

[5] T. Hayashi, W.-J. Song, J. Rose, Guided wave dispersion curves for a bar with an arbitrary cross-section, a rod and rail example, Ultrasonics 41 (3) (2003) 175–183.

[6] I. Bartoli, A. Marzani, F. Lanza di Scalea, E. Viola, Modeling wave propagation in damped waveguides of arbitrary cross-section, Journal of Sound and Vibration 295 (3-5) (2006) 685–707.

[7] V. Damljanović, R. Weaver, Propagating and evanescent elastic waves in cylindrical waveguides of arbitrary cross section, The Journal of the Acoustical Society of America 115 (4) (2004) 1572–1581.

[8] P. Loveday, Analysis of piezoelectric ultrasonic transducers attached to waveguides using waveguide finite elements, IEEE Transactions on Ultrasonics, Ferroelectrics and Frequency Controlultrasonics, ferroelectrics, and frequency control 54 (10) (2007) 2045 – 2051.

[9] P. Loveday, P. Wilcox, Guided wave propagation as a measure of axial loads in rails, in: SPIE conference proceedings, Vol. 7650, 2010, pp. 7650 – 7650 – 8.

[10] C. Chongyi, W. Chengguo, J. Ying, Study on numerical method to predict wheel/rail profile evolution due to wear, Wear 269 (3-4) (2010) 167–173.

[11] J. Gerlici, T. Lack, Railway wheel and rail head profiles development based on the geometric characteristics shapes, Wear 271 (1-2) (2011) 246–258.

[12] P. Wang, J. Xu, K. Xie, R. Chen, Numerical simulation of rail profiles evolution in the switch panel of a railway turnout, Wear 366-367 (2016) 105–115.

[13] M. Ignesti, M. Malvezzi, L. Marini, E. Meli, A. Rindi, Development of a wear model for the prediction of wheel and rail profile evolution in railway systems, Wear 284-285 (2012) 1–17.

[14] D. F. Cannon, K.-O. Edel, S. L. Grassie, K. Sawley, Rail defects: an overview, Fatigue and Fracture of Engineering Materials and Structures 26 (10) (2003) 865–886.

[15] I. I. Setshedi, Characterization of Rails Using Guided Wave Ultrasonic Measurements and the Semi-Analytical Finite Element Method, MEng Dissertation, University of Pretoria South Africa (2018).

[16] A. Cornish, Life-time monitoring of in service switches and crossings through field experimentation, PhD Thesis, Imperial College London (2014).

[17] U. Olofsson, T. Telliskivi, Wear, plastic deformation and friction of two rail steels - A full-scale test and a laboratory study, Wear 254 (1-2) (2003) 80–93.

[18] A. De Boer, M. Van Der Schoot, H. Bijl, New Method for Mesh Moving Based on Radial, in: European Conference on Computational Fluid Dynamics ECCOMAS, 2006, pp. 1–16.

[19] P. Loveday, C. Long, D. Ramatlo, Mode repulsion of ultrasonic guided waves in rails, Ultrasonics 84 (2018) 341–349.

[20] T. Ting, T. Chen, W. Twomey, Correlating mode shapes based on the modal assurance criterion, Finite Elements in Analysis and Design 14 (4) (1993) 353–360. doi:10.1016/0168-874X(93)90032-L.

[21] P. Welch, The use of Fast Fourier Transform for the estimation of Power Spectra: A method based on time averaging over short, modified periodograms, IEEE Transactions on Audio and Electroacoustic au-15 (2) (1967) 70–73.

[22] C. S. Long, P. W. Loveday, Prediction of guided wave scattering by defects in rails using numerical modelling, in: AIP Conference Proceedings, Vol. 1581, 2014, pp. 240–247.

[23] J. C. Helton, F. J. Davis, Latin hypercube sampling and the propagation of uncertainty in analyses of complex systems, Reliability Engineering and System Safety 81 (1) (2003) 23–69.

[24] MathWorks, Matlab r2018a and signal processing toolbox r2018a. (2018).
URL https://www.mathworks.com/help/signal/ref/findpeaks.html